Competition of Polar and Antipolar States Hidden Behind a Variety of Polarization Switching Modes in Hydrogen-Bonded Molecular Chains

Sachio Horiuchi,[*,†] Hiromi Minemawari,[†] and Shoji Ishibashi[‡]

[†]Research Institute for Advanced Electronics and Photonics (RIAEP), National Institute of Advanced Industrial Science and Technology (AIST), Tsukuba 305-8565, Japan

[‡]Research Center for Computational Design of Advanced Functional Materials (CD-FMat), National Institute of Advanced Industrial Science and Technology (AIST), Tsukuba 305-8568, Japan

Supporting Information

1. Thermal and Electric Properties

Thermal analysis was performed using a differential scanning calorimeter (DSC7000X; Hitachi High-Technologies, Tokyo). The sample was encapsulated in an aluminum pan and heated or cooled at 5 K/min. The temperature was calibrated to the melting point of indium (429.8 K).
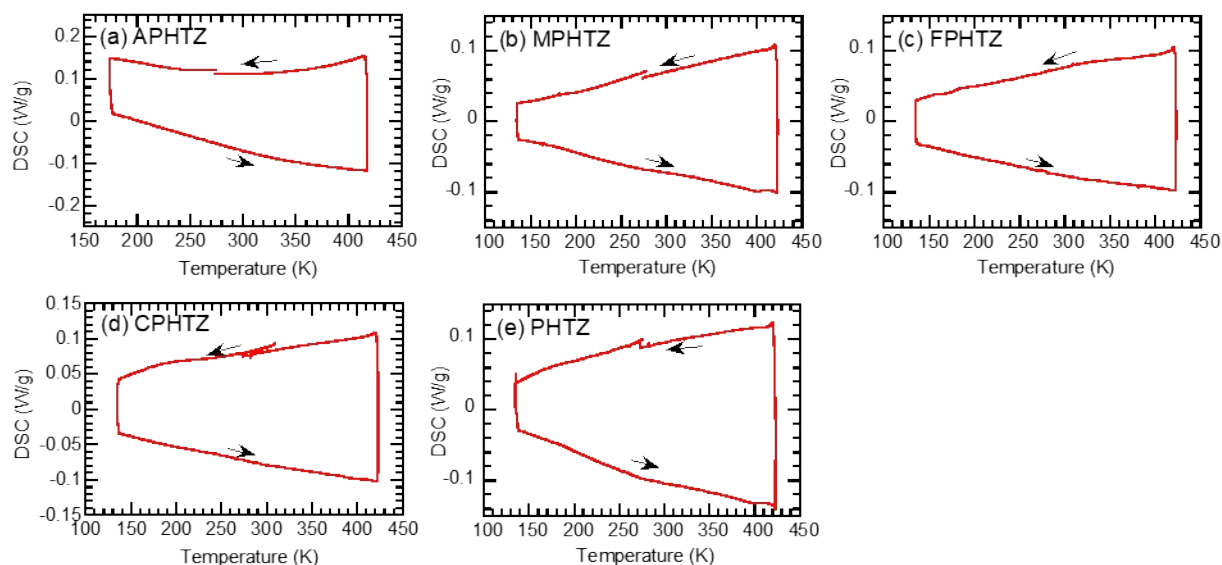

Figure S1. Differential scanning calorimetry (DSC) thermograms of (a) APHTZ, (b) MPHTZ, (c) FPHTZ, (d) CPHTZ, and (e) PHTZ crystals measured at a heating or cooling rate of 5 K/min. Baseline of data (b)–(e) is corrected by subtracting the data of the empty Al pan in the same temperature region.
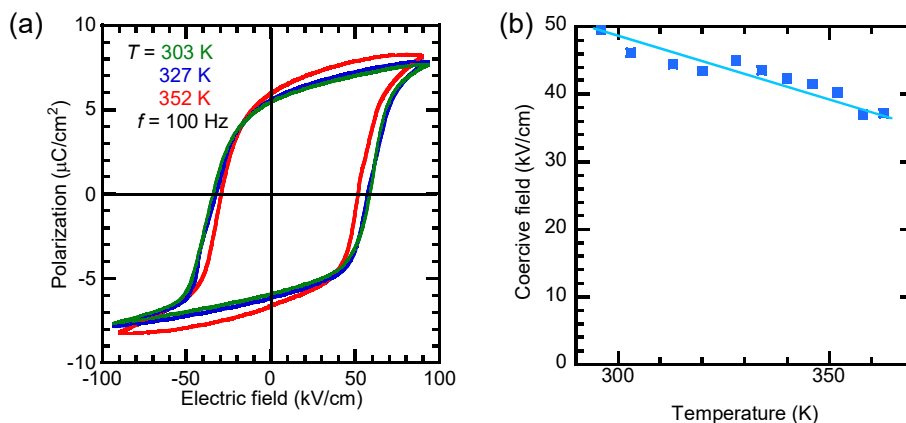

Figure S2. Polarization hysteresis of ferroelectric APHTZ. (a) *P-E* loops at selected temperatures. (b) Temperature variation of coercive fields.

Squaric acid (SQA) Furan-3,4-dicarboxylic acid (FDC) 3-(2-chlorophenyl)propiolic acid (CPPLA) 2-Phenylmalondialdehyde (PhMDA)

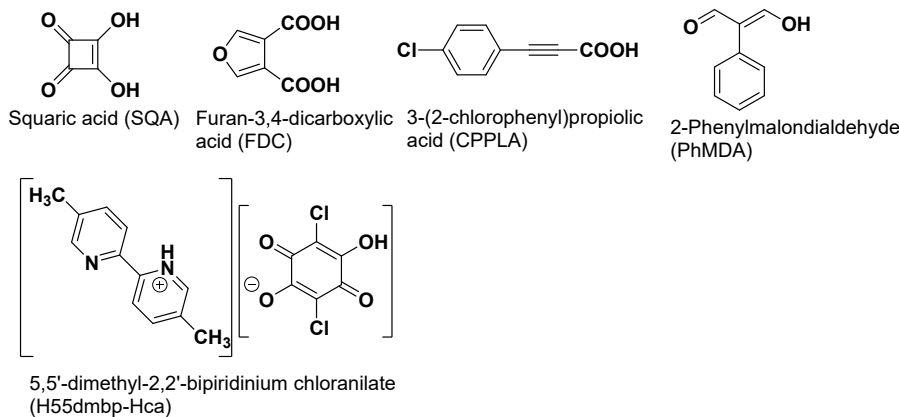5,5'-dimethyl-2,2'-bipiridinium chloranilate (H55dmbp-Hca)

Figure S3. Chemical structures of antiferroelectric organic crystals.

2. Structural and Theoretical Data Summary

Table S1 Crystal data and experimental details of phenyltetrazole and imidazole crystals.

	PHTZ	MPHTZ	APHTZ	FPHTZ
Chemical formula	$C_7H_6N_4$	$C_8H_8N_4$	$C_7H_7N_5$	$C_7H_5FN_4$
Formula wt.	146.15	160.18	161.17	164.14
Temperature (K)	296	296	296	296
a (Å)	9.8121(7)	9.7712(5)	8.2666(3)	8.0914(18)
b (Å)	15.2562(14)	9.0593(4)	5.6858(2)	5.9622(13)
c (Å)	4.5459(4)	17.7198(10)	15.5021(7)	14.789(4)
α (deg.)	90	90	90	90
β (deg.)	90	90	91.087(4)	92.037(5)
γ (deg.)	90	90	90	90
V (Å^3)	680.50(10)	1568.56(14)	728.50(5)	713.0(3)
Crystal system	orthorhombic	orthorhombic	monoclinic	monoclinic
Space group	$Ama2$(#40)	$Pbca$ (#61)	Pn (#7)	$P2_1/n$ (#14)
ρ_{calc} (g cm^{-3})	1.426	1.356	1.469	1.529
Z	4	8	4	4
Dimensions (mm)	0.50×0.46×0.12	0.42×0.35×0.12	0.35×0.30×0.08	0.55×0.29×0.10
Radiation	MoKα (0.7107 Å)	MoKα (0.7107 Å)	MoKα (0.7107 Å)	MoKα (0.7107 Å)
$2\theta_{max}$ (deg.)	55	55	55	55
R_{int}	0.014	0.016	0.020	0.019
Reflection used	756	1783	3133	1620
No. of variables	60	115	242	118
R $(2\sigma(I) < I)$	0.030	0.041	0.033	0.038
wR	0.073	0.141	0.085	0.109
GOF	1.05	1.09	1.04	1.06

	CPHTZ	TFPHTZ	DM-BIM	
Chemical formula	$C_7H_5ClN_4$	$C_8H_5F_3N_4$	$C_5H_7BrN_2$	
Formula wt.	180.60	214.15	175.03	
Temperature (K)	295	295	296	
a (Å)	9.457(3)	10.3316(19)	4.0674(3)	
b (Å)	11.427(3)	9.7732(16)	16.0311(8)	
c (Å)	7.298(2)	9.7411(18)	10.1239(5)	
α (deg.)	90	90	90	
β (deg.)	107.987(6)	116.898(3)	90	
γ (deg.)	90	90	90	
V (Å^3)	750.1(4)	877.2(3)	660.13(7)	
Crystal system	monoclinic	monoclinic	orthorhombic	
Space group	$P2/c$ (#13)	$P2_1/c$ (#14)	$Pbcm$ (#57)	
ρ_{calc} (g cm^{-3})	1.599	1.621	1.761	
Z	4	4	4	
Dimensions (mm)	0.35×0.30×0.20	0.2×0.2×0.2	0.46×0.25×0.21	
Radiation	MoKα (0.7107 Å)	MoKα (0.7107 Å)	MoKα (0.7107 Å)	
$2\theta_{max}$ (deg.)	55	55	55	
R_{int}	0.029	0.018	0.022	
Reflection used	1728	1982	804	
No. of variables	122	168	45	
R $(2\sigma(I) < I)$	0.040	0.045	0.027	
wR	0.117	0.132	0.075	
GOF	1.07	1.06	1.07	

Table S2 DFT calculations of phenyltetrazole crystals. Switchable polarizations $\Delta\mathbf{P}$ and their respective direction components. Energy difference ΔE of the ferro-/antiferro-electric states measured from the FE (or FE-I) states.

Compound-state [a] abbrev		Space Gr.	refcode [b]	ΔP_a	ΔP_b	ΔP_{c*}	$|\Delta\mathbf{P}|$	ΔE (meV/molecule)	Lattice transformation [c]
APHTZ	FE-I	Pn	†	7.529	0.000	-0.100	7.529	**0**	*
	FE-II	$P2_1$		0.000	4.951	0.000	4.951	+0.53	*
	AFE	C-1		–	–	–	–	+0.95	a'=2a, b'=2b, c'=c
	PE	$P2_1/n$	CITVIL	–	–	–	–	–	*
FPHTZ	FE-I	Pn		7.882	0.000	0.009	7.882	**0**	*
	FE-II	$P2_1$		0.000	5.879	0.000	5.879	+0.08	*
	AFE	C-1		–	–	–	–	-0.12	a'=2a, b'=2b, c'=c
	PE	$P2_1/n$	†	–	–	–	–	–	*
CPHTZ	FE	Pc		6.560	0.000	6.384	9.154	**0**	*
	AFE-I	P-1		–	–	–	–	+0.11	*
	AFE-II	$P2_1/c$		–	–	–	–	+0.24	a'=a, b'=2b, c'=c
	AFE-III	$P2_1/c$		–	–	–	–	+0.02	a'=a, b'=2b, c'=c, different orig.
	PE	$P2/c$	†,KUSLUG	–	–	–	–	–	*
MPHTZ	FE	$Pca2_1$		7.611	0.000	0.000	7.611	**0**	a''=c, b''=−½b, c''=a
	AFE-I	$Pbca$	†	–	–	–	–	-1.78	*
	AFE-II	$Pbca$		–	–	–	–	-0.58	*, different origin
	AFE-III	$P2_1/c$		–	–	–	–	+0.11	a'''=½b, b'''=c, c'''=a
	PE	$Pbcm$	QUCJII	–	–	–	–	–	a'=½b, b'=c, c'=a
PHTZ	FE	Cc	TOSJOA	9.190	0.000	-0.079	9.190	**0**	a'=c, b'=−b, c'=a
	AFE-I	$Pca2_1$		–	–	–	–	-0.96	a''=a, b''=b, c''=2c
	AFE-II	Pc		–	–	–	–	-0.91	a'''=½b−½c, b'''=−a, c'''=2c
	AFE-III	$Pna2_1$		–	–	–	–	-0.10	*
	PE	$Ama2$	†,TOSJOA01	–	–	–	–	–	*
PHIM	FE	Cc		9.366	0.000	-0.062	9.366	**0**	a'=c, b'=−b, c'=a
	AFE-I	$Pca2_1$		–	–	–	–	-4.26	a''=a, b''=b, c''=2c
	AFE-II	Pc		–	–	–	–	-4.17	a'''=½b−½c, b'''=−a, c'''=2c
	AFE-III	$Pna2_1$		–	–	–	–	-0.05	*
	PE	$Ama2$	OBUQUZ	–	–	–	–	–	*
TBIM	FE	Cc		10.850	0.000	0.017	10.850	**0**	a'=c, b'=−b, c'=a
	AFE-I	$Pca2_1$		–	–	–	–	-3.42	a''=a, b''=b, c''=2c
	AFE-II	Pc		–	–	–	–	-3.42	a'''=½b−½c, b'''=−a, c'''=2c
	AFE-III	$Pna2_1$		–	–	–	–	+0.88	*
	PE	$Ama2$	BOWROW	–	–	–	–	–	*
DM-BIM	FE	$Pca2_1$		0.000	0.000	11.305	11.305	**0**	a'=b, b'=−a, c'=c
	AFE-I	$Pbca$		–	–	–	–	-3.96	a''=c, b''=2a, c''=b
	AFE-II	$Pbca$		–	–	–	–	-3.86	a''=c, b''=2a, c''=b, different orig.
	AFE-III	$P2_1/c$		–	–	–	–	+0.41	*
	PE	$Pbcm$	†	–	–	–	–	–	*

a) "PE" denotes the paraelectric-like prototypical structure with disordered hydrogen bonds.
b) See below for the CSD refcodes for deposited structures.   † This work.
c) For each compound, the (a, b, c) axes defined on the structures indicated by asterisks are employed as the direction basis for the calculated $\Delta\mathbf{P}$.

References

CITVIL) Y. Zou, S. Hong, M. Park, H. Chun, and M. S. Lah, *Chem. Commun.* 2007, 5182.
KUSLUG) L. Xu, L.-Y. Gu, D.-Y. Zhao, B. Wang, T.-G. Kang, *Acta Crystallogr. E*, 2010, **66**, o742.
QUCJII) D.-Y. Hu, X.-W. Chu, Z.-R. Qu, *Acta Crystallogr. E*, 2009, **65**, o2463.
TOSJOA) T. M. Krygowski, M. Cyranski, *Tetrahedron* 1996, **52**, 10255.
TOSJOA01) R. E. Marsh, *Acta Crystallogr.,Sect.B:Struct.Sci.* 2004, **60**, 252.
BOWROW) M. Andrzejewski, J. Marciniak, K. W. Rajewski, A. Katrusiak, *Cryst. Growth Des.* 2015, **15**, 1658.
OBUQUZ) M. M. Barforoush, S. Naderi, A. R. Ghanbarpour, A. A. Tehrani, H. R. Khavasi, *Acta Crystallogr., Sect.E: Struct. Rep. Online* 2011, **67**, o3248.

3. Structural and Theoretical Properties of PHTZs
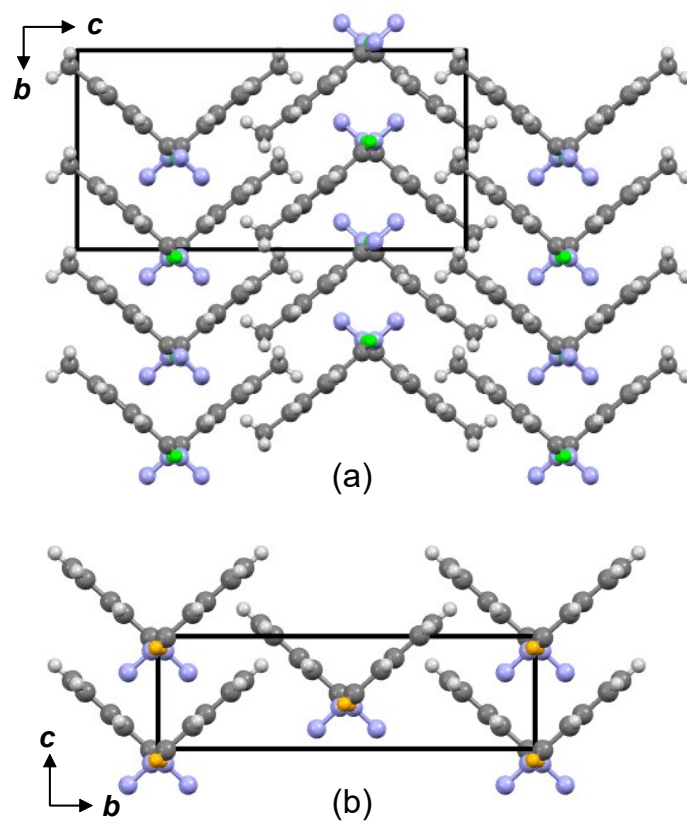

(a)

(b)

Figure S4 Crystal structures of antiferroelectric compounds. Molecular packings of (a) MPHTZ and (b) PHTZ crystals viewed along the crystallographic *a*-directions. Green and orange balls are ordered and disordered hydrogen atoms, respectively.
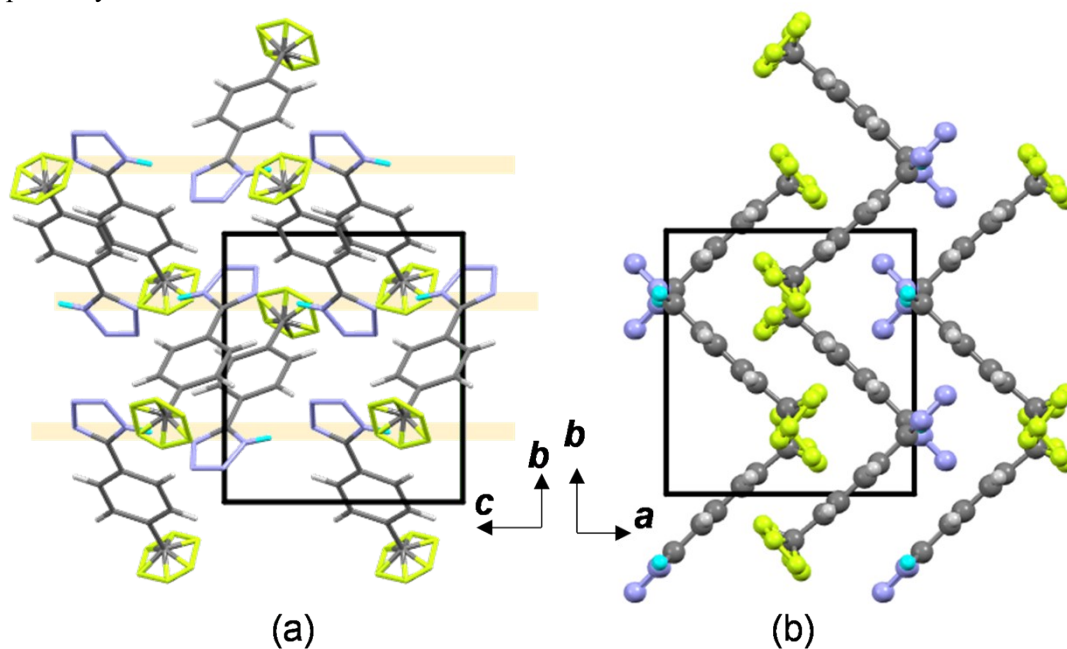

(a)   (b)

Figure S5 Crystal structures of TFPHTZ viewed along the crystallographic (a) *a*- and (b) *c*-directions. Orange ribbons and blue balls represent hydrogen-bonded molecular sequences and disordered hydrogen atoms, respectively.
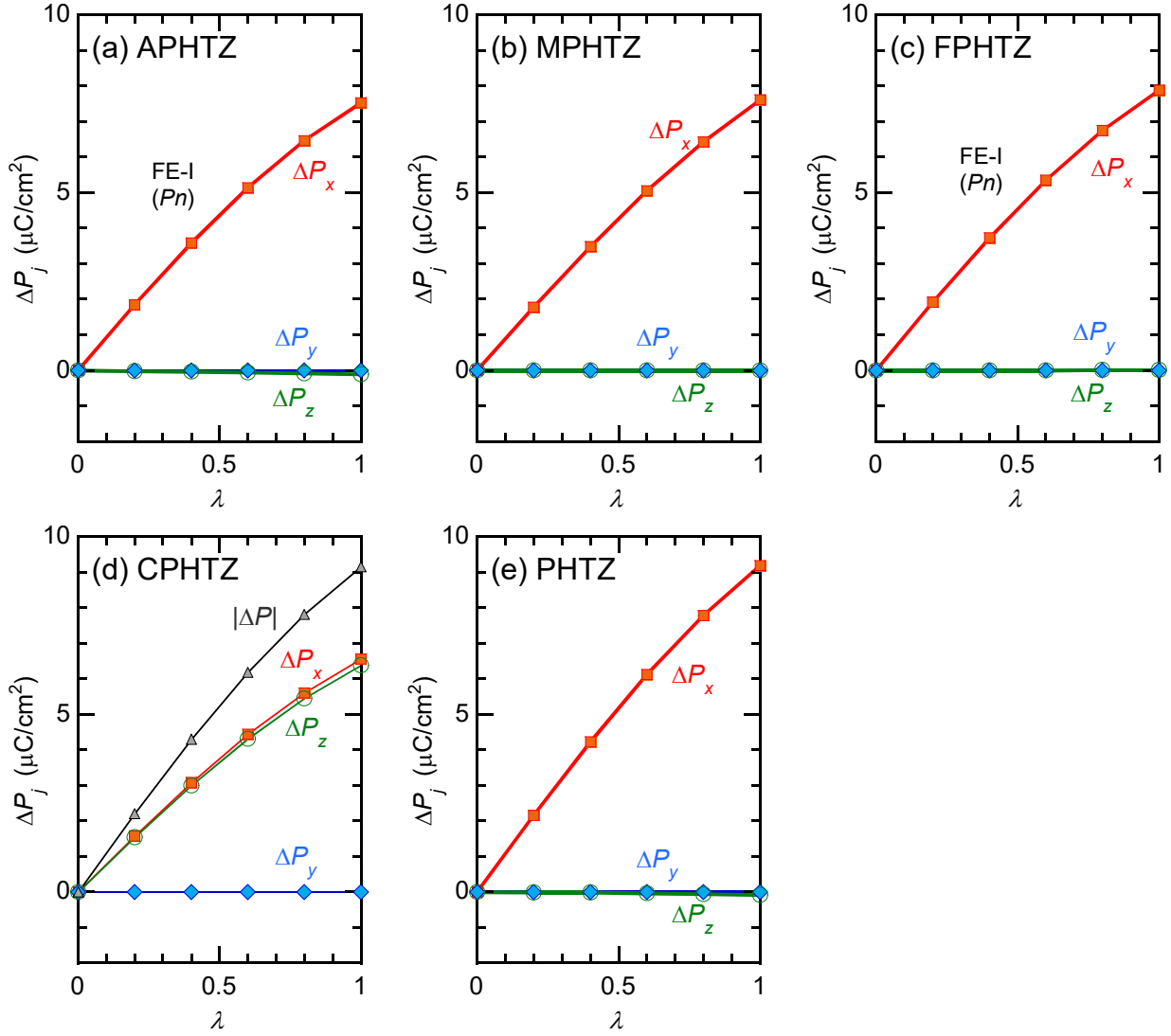
Figure S6 Evolution of polarization change $\Delta\boldsymbol{P}$ in the ferroelectric form of (a) APHTZ, (b) MPHTZ, (c) FPHTZ, (d) CPHTZ, and (e) PHTZ as a function of the degree of polar distortion λ, which ranges from the symmetrized reference (hypothetical paraelectric, $\lambda = 0$) to the fully polarized (ferroelectric, $\lambda = 1$) configuration. Cartesian coordinate system (x, y, z) is parallel to the crystallographic $(\boldsymbol{a}, \boldsymbol{b}, \boldsymbol{c}^*)$ axes for the monoclinic APHTZ, FPHTZ, and CPHTZ crystal, and parallel to the $(\boldsymbol{a}, \boldsymbol{b}, \boldsymbol{c})$ axes of orthorhombic ($Pbca$ and $Ama2$) forms for MPHTZ ($Pbca$) and PHTZ crystals ($Ama2$).

FE (*Pc*)

AFE-I (*P*-1)

AFE-II (*P2₁/c, a'=a, b'=2b, c'=c*)

AFE-III (*P2₁/c, a'=a, b'=2b, c'=c*; different origin)
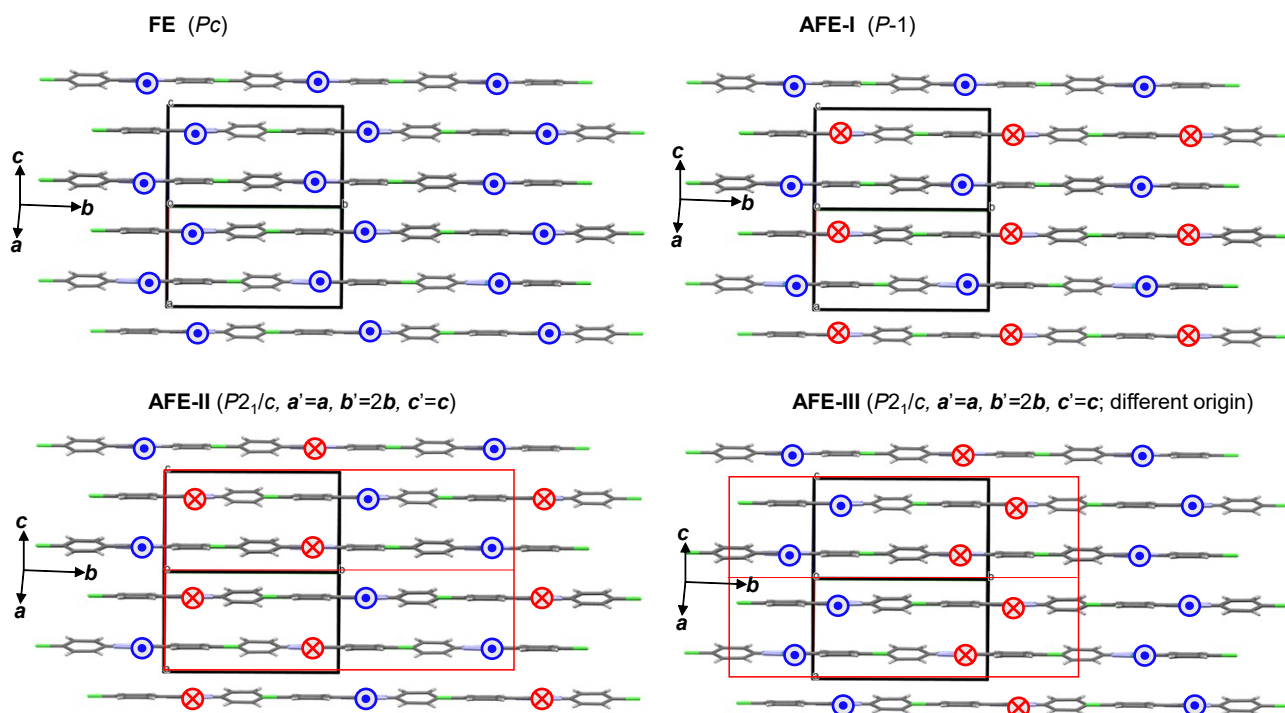
Figure S7   Schematic arrangements of switchable dipole moments (arrows) in candidate ferroelectric and antiferroelectric structural forms of the CPHTZ crystal. Unit cell (black squares) corresponds to the [101]-projection of the (*a*, *b*, *c*) axes of the fundamental monoclinic (*P2/c*) structure. New space group and required transformation (if necessary) to the new unit cell (red squares) are noted at the top of each panel.

4. Structural and Theoretical Properties of Imidazoles

(a)   (b)   (c)
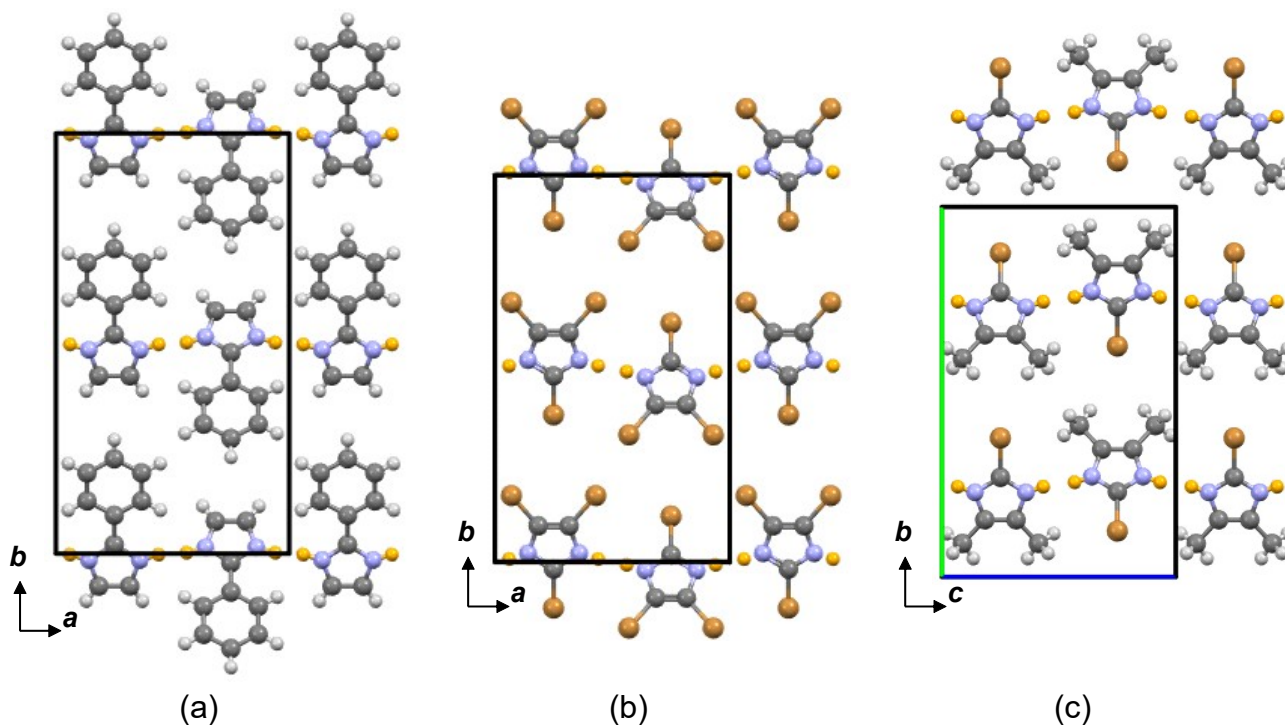
Figure S8   Crystal structures of (a) PHIM, (b) TBIM, and (c) DM-BIM viewed along the molecular stacking direction. Orange balls represent disordered hydrogen atoms.
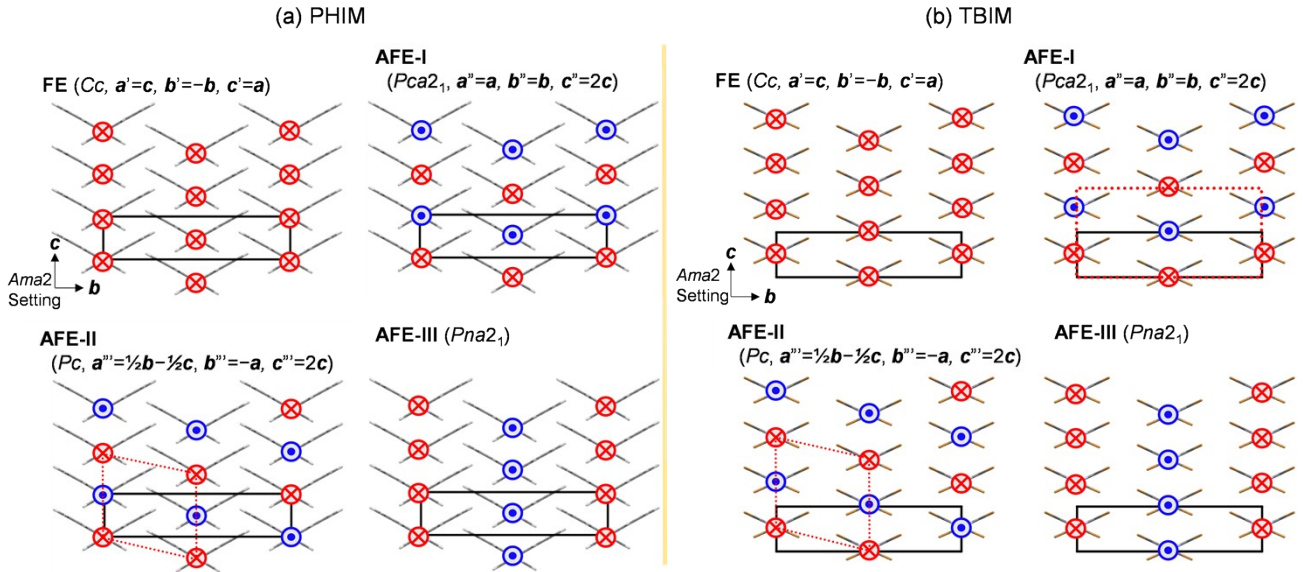
Figure S9 Schematic arrangements of switchable dipole moments (arrows) in candidate ferroelectric and antiferroelectric structural forms of (a) PHIM and (b) TBIM crystals. Open rectangles define the *a*-axis projection of the (*a*, *b*, *c*) axes of the fundamental orthorhombic (*Ama2*) structure. New space group and required transformation (if necessary) to the new unit cell (red dotted squares) are noted at the top of each panel.
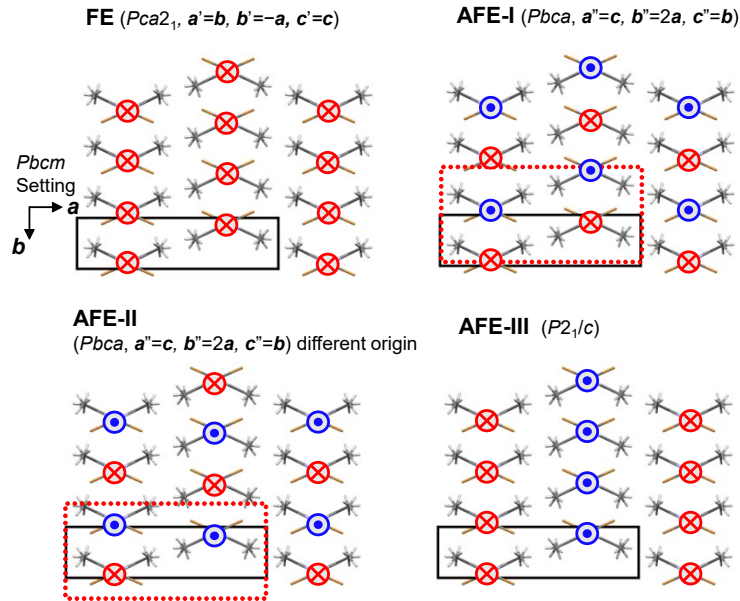

Figure S10 Schematic arrangements of the switchable dipole moments (arrows) in the candidate ferroelectric and antiferroelectric structural forms of the DM-BIM crystal. Open rectangles define the *a*-axis projection of the (*a*, *b*, *c*) axes of the fundamental orthorhombic (*Pbcm*) structure. New space group and required transformation (if necessary) to the new unit cell (red dotted squares) are noted at the top of each panel.
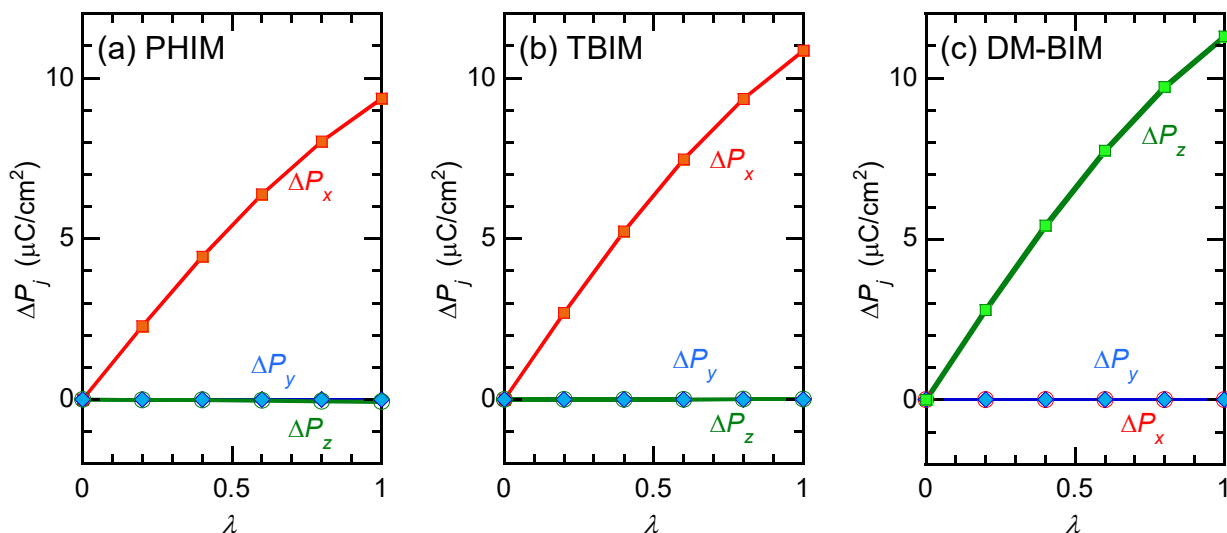
Figure S11 Evolution of polarization change ΔP in the ferroelectric form of (a) PHIM, (b) TBIM, and (c) DM-BIM as a function of the degree of polar distortion λ, which ranges from the symmetrized reference (hypothetical paraelectric, $\lambda = 0$) to the fully polarized (ferroelectric, $\lambda = 1$) configuration. Cartesian coordinate system (x, y, z) is parallel to the crystallographic ($\boldsymbol{a}$, $\boldsymbol{b}$, $\boldsymbol{c}$) axes for the orthorhombic ($Ama2$) form for PHIM and TBIM crystals and parallel to the ($\boldsymbol{a}$, $\boldsymbol{b}$, $\boldsymbol{c}$) axes of orthorhombic ($Pbcm$) for the DM-BIM crystal.
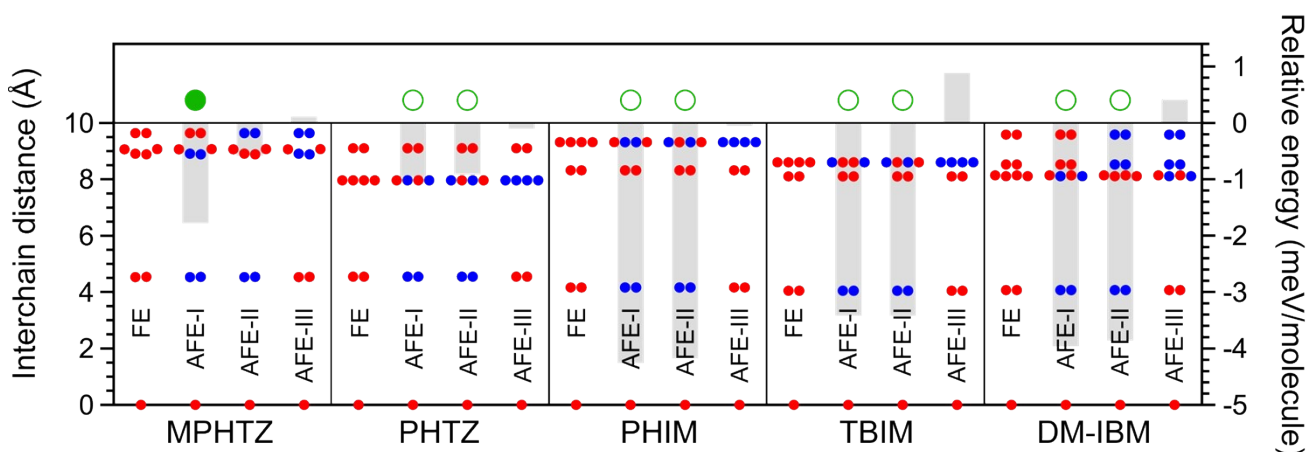

Figure S12 Distribution of the interchain distances within 10 Å for neighboring chains with parallel (red circles) and antiparallel switchable polarities (blue circles) in candidate FE and AFE states of MPHTZ, PHTZ, PHIM, TBIM, and DM-BIM. Shaded histogram represents the energy of candidate H-ordered states relative to each FE (or FE-I) form. Filled and open circles point to non-degenerate and nearly degenerate ground states, respectively. These five compounds have very simple crystal symmetry: each NH···N bond center (carrying the electric dipole) occupies the orthorhombic primitive lattice. Therefore, the effects of the interchain dipole-dipole interactions can be compared simply as a function of the interchain distances. Given the same interchain distance, the interchain antiparallel dipole-dipole interactions are more favorable than the parallel ones. Indeed, the most stable AFE-I states and the next stable AFE-II ones adopt antipolar dipoles at the first nearest distance. In contrast, the interactions with the second nearest chains cause the energy difference between the AFE-I and AFE-II states in the MPHTZ crystals: antiparallel ones stabilize the AFE-I state while parallel ones destabilize the AFE-II state. For the PHTZ crystal, the degeneracy of the AFE-I and AFE-II states can be attributed to almost the same distributions of parallel and antiparallel chains at the second and third nearest distances. Similar explanations can be applied to the degeneracy in the three imidazole crystals in which the first nearest chains at the shorter distances likely cause the larger energy difference between the FE and AFE-I states compared with the PHTZ crystal. These observations indicate that the dipole-dipole interactions play critical roles in determining the observed phase stabilities.

5. Supplementary Discussion on the Phase Stability

The actual phase transformation requires additional cost for the nucleation and expansion of domains accompanied by a pair of domain walls with opposite bound charges on chains. New domains can expand spontaneously only when their length exceeds the critical one at which the energy gain of phase transformation is balanced with the attractive Coulombic force of each domain wall pair. This critical domain length is roughly estimated to involve from several to more than ten molecules, the number of which depends on the magnitudes of energy gain and ferroelectric polarization.

The observation of hysteresis in *P-E* curve manifests itself that the assist of external field (i.e. electric energy gain at the onset of switching) is required to trigger the motion of the domain walls. In the APHTZ crystal, the switching from FE(-) to FE(+) state starts under $E_{sw} \sim 10$ kV/cm, at which the FE(+) state becomes stable by $2P_sE_{sw}$ ~ 0.16 meV/molecule relative to the FE(-) state by taking the difference of polarization ($2P_s \sim 14$ μC/cm^2) into consideration. On the other hand for the switching from ferroelectric FE(-) to antipolar AFE state, the charge density at the domain boundary is just the half that of the ferroelectric polarization reversal and then will reduce the electrostatic cost (by quarter for the lowest). As shown in the schematic energy diagram in Figure S13(a), the switching from the FE(-) to (metastable) AFE state may proceed before the polarization switching to FE(+) state unless the energy ΔE of antipolar state exceeds +0.04 meV/molecule. The lower limit of ΔE (-0.16 meV/molecule) is derived at the situation where the FE state is barely metastable at zero field and the electrostatic cost is assumed to be negligible in formation/dynamics of domain walls, as shown in Figure S13(b). The $\Delta E = -0.12$ meV/molecule for FPHTZ falling on this range can reasonably explain the experimental observations of double hysteresis loops together with the metastable ferroelectric state. On the other hand, the $\Delta E = 0.53$ meV/molecule obtained from the for APHTZ is far above this ΔE range even considering the computational resolution (< 0.3 meV/molecule) (Figure S13 (c)). This result apparently excludes the emergence of antipolar states and then consistent with experimental observation.
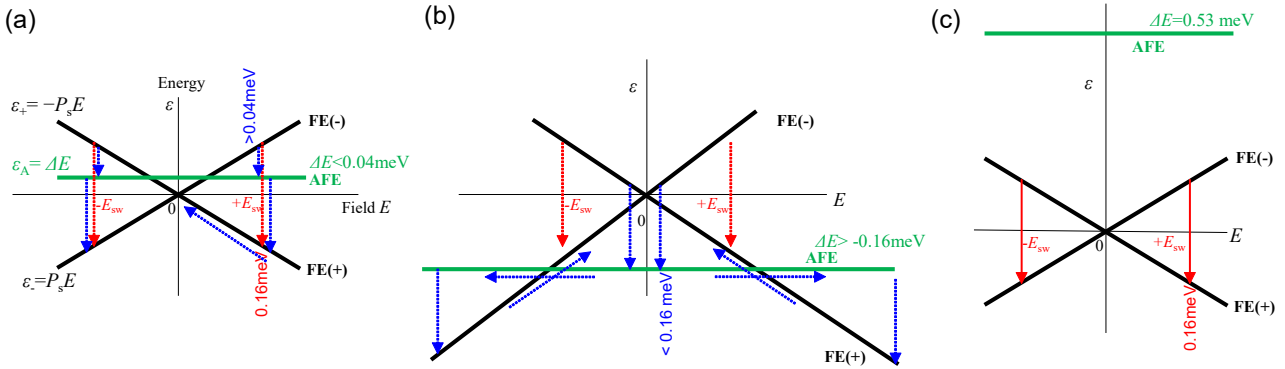

Figure S13 Schematic energy diagram demonstrating the requirement for ΔE for F/A-hybrid state permitting FE-to-AFE switching before the ferroelectric polarization reversal. Solid (dotted) red arrows indicate the proper (hypothetical) ferroelectric polarization reversal. The dotted blue arrows show the paths for expected FE-AFE phase transformations. Panels (a) and (b) correspond to the situations of upper and lower limits of ΔE, respectively. (c) Diagram for the ferroelectric APHTZ crystal.